Contents lists available at ScienceDirect

Journal of Hazardous Materials Advances

journal homepage: www.elsevier.com/locate/hazadv

Feasibility of sugarcane bagasse/polydopamine as sustainable adsorbents for Cr(VI) with reusability in cement composition

Mário A.B.S. Nunes [a], Dairon P. Fuentes [a], José A.F.S. Mesquita [b], Roberto C.O. Romano [b], Rafael G. Pileggi [b], Pedro V. Oliveira [a], Denise F.S. Petri [a,*]

[a] *Institute of Chemistry, University of São Paulo, Av. Prof. Lineu Prestes 748, São Paulo 05508-000, Brazil*
[b] *Department of Civil Construction Engineering, University of São Paulo, Av. Prof. Luciano Gualberto 380 – São Paulo, São Paulo 05508-010, Brazil*

ARTICLE INFO

Keywords:
Sugarcane bagasse
Polydopamine
Cr(VI) ions
Adsorption
Cement
Circular economy

ABSTRACT

The removal of pollutants from water should be followed by a proper treatment of the spent adsorbents. In this study, sugarcane bagasse/polydopamine (SB/PDA) adsorbents were applied in batch and column adsorption studies towards Cr(VI) ions. Adsorbents prepared with higher concentration of dopamine (4 $g.L^{-1}$) led to more efficient adsorbents (SB/PDA4) and maximum adsorption capacity (q_{max}) of 138 $mg.g^{-1}$. X-ray photoelectron spectroscopy (XPS) analyses revealed that the adsorption mechanism involved ion-dipole and electrostatic interactions between Cr(VI) and the PDA functional groups. The spontaneous (ΔG_{ads} - 9 kJ mol^{-1}) adsorption process was driven by an entropic gain related to the release of counter-ions and water molecules. Under optimized operational conditions, the maximum adsorption capacity in the fixed-bed column achieved the adsorption capacity of 141.7 $mg.g^{-1}$. Considering the circular economy principles, the contaminated adsorbents were incorporated to cement pastes. No leaching of Cr(VI) from the cement/adsorbent samples could be detected over 64 days, and their mechanical behavior was comparable to the reference cement samples. The efficient removal of Cr(VI) from wastewater by SB/PDA adsorbents and the successful incorporation of spent adsorbents to cement demonstrated a sustainable management of liquid and solid wastes.

1. Introduction

The environment and human health are under significant threat from water pollution caused by heavy metals (Fu and Wang, 2011). Hexavalent chromium is one of the most severe inorganic pollutants, commonly found in various human-made activities such as mining, metallurgy, tannery, and textile dying (Rajapaksha et al., 2022). If the wastewater from these processes is not treated, the final destination of Cr(VI) ions may be natural waters. Chromium exists in a series of oxidation states from −2 to +6 valence, but the most common states are the Cr(III) and Cr(VI). Cr(III) is a vital trace element for glucose metabolism, whereas Cr(VI) can cause significant toxicity, carcinogenicity, and mutagenicity to humans and other living organisms (Bagchi et al., 2002).

Wastewater can be treated by physical, microbiological, oxidative, and chemical methods, and phytoremediation (Kesari et al., 2021). Each method has its peculiarity regarding effectiveness, secondary pollution, operational and maintenance costs, and applicability on a large scale (Alsawy et al., 2022). Adsorption is a very promising strategy because the adsorbents can be chemically modified to increase the adsorption efficiency, the optimization of the adsorption parameters allows its application on a large scale, and there is a plethora of sustainable (Khan et al., 2021) and emerging materials (Xu et al., 2021) that can be transformed into adsorbents. Lignocellulosic materials are abundant and contain functional groups (hydroxyl, carboxylic acid, aromatic rings) that make them interesting for the removal of heavy metals from wastewater (Sharma et al., 2022). Sugarcane bagasse (SB) is an agro-waste consisting of cellulose, hemicellulose, and lignin, which have multiple functional groups (hydroxyl, carboxylic acid, aromatic rings) acting as adsorption sites (Sarker et al., 2017). However, due to the intrinsic recalcitrance (Zoghlami and Paës, 2019), the functional groups present on the surface are not fully available, requiring a modification to increase the metal uptake capacity. Polydopamine (PDA) is an excellent option to solve this shortcoming, due to its super-adhesion properties (Ryu et al., 2018) and various functional groups present on its structure such as hydroxyl, amine, carboxyl, quinone, and imine, that can strongly

---

* Corresponding author.
E-mail address: dfsp@iq.usp.br (D.F.S. Petri).

https://doi.org/10.1016/j.hazadv.2023.100366
Received 5 June 2023; Received in revised form 8 August 2023; Accepted 26 August 2023

bind to metal ions (Gao et al., 2013; Wang et al., 2020) and to polysaccharides (Liu et al., 2022).

Although the adsorption process is efficient to remove pollutants from wastewater, the fate of the spent adsorbents is still challenging because they are usually incinerated or landfilled (Mohan and Pittman, 2007). The toxic characteristics of the post-adsorption material require stabilization of the adsorbent before landfilling (Nasruddin et al., 2018). Discarding the adsorbent after a single use is often viewed as the primary disadvantage of adsorption, particularly when the regeneration is not economically or environmentally viable (Furtado et al., 2020). Metal ions enriched adsorbents can be reused in energy storage devices or catalyst support (Baskar et al., 2022), or they can be added to cementitious materials (Simón et al., 2022; Zein et al., 2022) trying to promote a chemical fixation of leachable ions in the hydrated matrix of cement products. The poor permeability of the cement matrices can also help to reduce the mobility and leachability of heavy metal ions, decreasing the toxicity of the contaminants (Chen et al., 2009). There is a plethora of reports about the incorporation of agricultural waste ashes to building materials (Ahmad et al., 2021; Charitha et al., 2021; Jittin and Bahurudeen, 2022). However, there are few studies (Simón et al., 2022; Zein et al., 2022) about the inclusion of agricultural waste contaminated with heavy metals to cement-based materials.

PDA particles (Xiang et al., 2020; Zhang et al., 2018) and PDA deposited on cellulose nanocrystals (CNCs) (Dong et al., 2019) were already reported as adsorbents for Cr(VI) ions in batch adsorption studies. The novelty of this work is (i) the preparation of sugarcane bagasse/polydopamine (SB/PDA) adsorbents varying the dopamine concentration, to be applied as highly-efficient Cr(VI) adsorbents in batch and column adsorption studies, and (ii) the incorporation of the spent adsorbents to cement pastes. Promoting the functional use of the spent adsorbents is an unusual approach, since most of the researches do not account the pollution generated by the contaminated adsorbent as a relevant topic. For the batch adsorption studies, the effect of pH, adsorbate concentration, contact time, adsorbent dosage, temperature, and coexisting ions on the adsorption behavior was systematically evaluated. The column adsorption operational parameters (mass of adsorbent, flow rate, initial concentration) were optimized and applied for Cr(VI) solutions prepared with natural freshwater. Then, the spent adsorbents were applied to produce cement-based materials. The leachability of Cr(VI) ions, mechanical, and morphological properties of the cement products were evaluated. By minimizing the disposal of spent adsorbents, a secondary contamination could be avoided and more sustainable processes can be achieved.

2. Experimental

2.1. Materials

Dopamine hydrochloride (DA, Sigma H8502, 189.64 g.mol^{-1}, 98%), and tris-HCl buffer solution (Sigma 10,812,846,001, 157.60 g.mol^{-1}, 99%) were used as received. The reagents employed to adjust the medium pH were HCl (Synth, 36.46 g.mol^{-1}, 99%), and NaOH (Synth, 40 g.mol^{-1}, 97%). A standard solution of Cr(VI) at 2.50 g.L^{-1} was prepared dissolving $K_2Cr_2O_7$ (Synth, 294.18 g/mol, 99%) in 0.01 mol.L^{-1} HNO_3.

Sugarcane bagasse (SB), a waste from a local market, was rinsed with tap water, dried, ground in a knife mill (Willye, TE-680, TECNAL), and sieved through a 400 μm mesh vibratory sieve shaker (Retsch AS 200, Germany). The SB microparticles were exhaustively rinsed with distilled water (~ 100 mL water for each gram of SB), and dried in an oven at 60 °C overnight. The particle size distribution indicated a bimodal size distribution with mean sizes of 105 μm (13.5%) and 339 μm (86.5%), as reported elsewhere (Novaes et al., 2022). The contents of holocellulose, lignin, and ash in the SB amounted to 79.0, 20.5, and 0.2%, respectively (Novaes et al., 2022).

2.2. SB/PDA adsorbent synthesis

DA was dissolved in 10 mM Tris–HCl buffer (pH 8.5) at 2.0 g.L^{-1} or 4.0 g.L^{-1}. Then SB microparticles were added at 0.5 g.L^{-1}. The system was kept under magnetic stirring at 22 °C, during 4 h, until the complete oxidation of DA to PDA (Furtado et al., 2022, 2020). After that, the particles settled to the bottom of the vial, and the supernatant was removed. After drying overnight at 80 °C, the materials were coded as neat SB, SB/PDA2, and SB/PDA4.

2.3. Batch adsorption studies

Kinetic adsorption experiments were performed for Cr(VI) at 150 mg.L^{-1} (pH 2), on SB/PDA2 and SB/PDA4, under shaking at (22 ± 1) °C, and contact time of 5, 10, 15, 20, 25, 30, 40, 50, and 60 min. The adsorption isotherms of Cr(VI) on SB/PDA2 and SB/PDA4 were performed at (22 ± 1) °C. A fixed amount of adsorbent (10 mg) was added to 4 mL of Cr(VI) solution (pH 2), in the concentration range from 50 mg.L^{-1} to 250 mg.L^{-1}. The vials were kept under shaking for 60 min. To evaluate the effect of pH on the adsorption capacity, 10 mg of adsorbent was added to 4 mL of Cr(VI) solution at 150 mg.L^{-1} prepared at pH 2, 4, 6, or 8, and (22 ± 1) °C. The pH was adjusted either with 0.1 mol.L^{-1} HCl or 0.1 mol.L^{-1} NaOH. The vials were kept under shaking for 60 min. The effect of temperature on the adsorption of Cr(VI) on SB/PDA2 and SB/PDA4 was evaluated at 299.3 K, 304.6 K, and 309.4 K. A fixed amount of adsorbent (10 mg) was added to 4 mL of Cr(VI) solution prepared at 150 mg.L^{-1} (pH 2); the vials were kept under magnetic stirring for 60 min. One should notice that the adsorption capacity of neat SB microparticles towards Cr(VI) ions was too low and for this reason, they were not further used for the systematic adsorption studies. After the batch adsorption experiments, the systems were centrifugated (3200 rpm = 688.12 g) for 5 min. Then, the adsorbent was removed and dried in an oven at 60 °C during 24 h, and the concentration of Cr(VI) ions remaining in the supernatant was determined by measuring the absorbance at 350 nm (Beckman-Coulter DU650 spectrophotometer). A calibration curve was used to determine the concentration of Cr(VI) ions in the supernatant at equilibrium (C_e) (**Supplementary Material SM1**). To ensure the reliability, reproducibility, and precision of the measured data, all experiments were repeated at least twice.

The equilibrium adsorption capacity (q_e, mg/g) was calculated dividing the concentration of adsorbed Cr(VI) ions ($C_0 - C_e$) by the mass of dried adsorbent (m) and multiplying by the solution volume (V):

$$q_e = \frac{C_0 - C_e}{m} \times V \tag{1}$$

where C_0 and C_e are the initial concentration and the concentration at the equilibrium, respectively.

The removal capacity (Removal%) was calculated as

$$\text{Removal } (\%) = \frac{C_0 - C_e}{C_0} \times 100 \tag{2}$$

2.4. Fixed-bed column studies

Column adsorption experiments were conducted using polyethylene columns of 0.67 cm diameter and 6 cm long ((Eichrom Technologies Inc., Darien, USA), coupled to silicone Tygon® tubes attached to a peristaltic pump, at 22 °C, as presented in the **Supplementary Material SM2**. The adsorbent microparticles were packed in the column containing a frit at the bottom and at the top to avoid leakage to the outlet (**Supplementary Material SM2**). To optimize the operational parameters, the adsorbent (SB/PDA2 or SB/PDA4) mass (m, 50, 100, 200, and 500 mg), the initial Cr(VI) solution concentration (C_0, 75 mg.L^{-1} and 150 mg.L^{-1}), and the flow rate (ν, 0.8 mL.min^{-1} and 1.5 mL.min^{-1}) were varied. The pH 2 was kept constant in all experiments.

The effect of the presence of Ca^{2+} and Mg^{2+} ions at 5 mg.L^{-1} (each)

Table 1

. Compositions of the cementitious pastes with the respective codes and the tests performed for each of them. TS and SEM stand for tensile strength and scanning electron microscopy, respectively. The control sample (no spent adsorbent added) was coded as REF.

Code	Mass (g)			Characterization		
	Cement	Water	Adsorbent	SEM	Leaching	TS
REF	50.0	25.0	0	X	X	X
SB/0.1	47.5	23.8	0.08	–	X	–
SB/0.2	45.0	22.6	0.16	–	X	–
SB/0.5	40.0	20.2	0.33	X	X	X
SB/PDA/Cr/0.1	47.5	23.8	0.08	–	X	–
SB/PDA/Cr/0.2	45.0	22.6	0.16	–	X	–
SB/PDA/Cr/0.5	40.0	20.2	0.33	X	X	X

on the adsorption of Cr(VI) ($C_0 = 20$ mg.L^{-1}) onto SB/PDA4 was evaluated at pH 2 and flow rate of 3 mL.min^{-1}. The inductively coupled plasma optical emission spectrometry (ICP OES) technique was used for the simultaneous quantification of chromium, calcium, and magnesium in the eluate from the column. The breakthrough curves in presence of Ca^{2+} and Mg^{2+} were obtained online by coupling the eluate from the column directly to the spectrometer. For this, an optical emission spectrometer, model iCAP 7400 Duo, with radial and axial view, CID (Charge Injection Device) detector, which allows coverage wavelength from 166.4 to 847.0 nm a focal length of 383 mm that provides an optical resolution from 19 pm to 200 nm, Echelle polychromator with 52.91 mm^{-1} lines and 27.12 MHz radiofrequency sources, being able to adjust the applied power from 750 to 1350 W was used. Argon (99.998% v/v) was used to generate and maintain the plasma and aerosol introduction. **Supplementary Material SM3** shows the instrumental parameters of ICP OES for the simultaneous online determination of Cr, Ca, and Mg.

The column adsorption experiments were also performed for Cr(VI) ions dissolved in freshwater (pH = 7, ionic conductivity = 140 μS/cm) collected from a dam located inside the university campus (**Supplementary Material SM4**). The UV–Vis spectrum (**Supplementary Material SM4**) of the natural freshwater indicated the possible presence of nitrate and carbonate ions, and organic molecules (humic and fulvic acids). The column adsorption experiments were performed with SB/PDA4 ($m = 100$ mg), $C_0 = 150$ mg.L^{-1}, $\nu = 1.5$ mL.min^{-1}. For comparison, column adsorption experiments were done under the same conditions, but some droplets of concentrated HNO_3 was added to the Cr (VI) solution to decrease the pH to 2. The eluents that came out of the column were analyzed by UV–Vis after subtracting the blank run with the freshwater.

2.5. Characterization of the adsorbents

Scanning electron microscopy (SEM) analyses were performed for gold-sputtered samples in a Jeol Neoscope microscope JCM 5000 operating at a voltage of 10 kV. Atomic force microscopy (AFM) analyses were carried out in a Multimode 8 Bruker, in the tapping mode, in the air, using Si_3N_4 tips with spring constant of 0.4 N m^{-1}. Fourier transform infrared (FTIR) vibrational spectroscopy analyses were performed in the attenuated total reflectance (ATR) mode, using a Perkin Elmer Frontier equipment with resolution of 4 cm^{-1} and in the spectral range of 600 to 4000 cm^{-1}, with accumulation of 32 scans. X-ray photoelectron spectroscopy (XPS, K-Alpha spectrometer, Thermo Fisher Scientific, UK) analyses were performed for SB/PDA2 and SB/PDA4 before and after adsorption of Cr(VI), using the software CasaXPS to quantify the fraction of each element. Elemental analyses (CHN) of dried adsorbent samples were performed using a Perkin Elmer 2400 series ii elemental analyzer. The BET (Brunauer/Emmett/Teller) N_2 adsorption−desorption isotherms were determined for dried adsorbent samples in duplicate using a BelSorp equipment from Bel Japan (details in the **Supplementary Material SM5**).

2.6. Production of cement-based material with spent adsorbents

All spent adsorbents (SB/PDA2 and SB/PDA4) were put together and dried in an oven at 60 °C during 24 h. The purest Brazilian Portland cement (CPV, equivalent to a CEM I for European standard, or Type III for US Standard) was chosen and the pastes were produced maintaining the water-to-cement ratio (w/c) of 0.5, and using deionized water. The cement composition is described in the **Supplementary Material SM6**. The content of spent adsorbent was varied as shown in Table 1. The pastes were mechanically dispersed at 1500 rpm for 120 s using a Hauschild speed mixer. After that, polystyrene or polydimethylsiloxane molds were filled with the pastes. Neat SB and SB/PDA presented a density of ~ 0.10 g.cm^{-3} (Junior et al., 2017). For the leaching assays, the pastes prepared with 0.11 wt%, 0.24 wt%, and 0.55 wt% of spent adsorbents, were coded as SB/PDA/Cr/0.1, SB/PDA/Cr/0.2, and SB/PDA/Cr/0.5 (Table 1), respectively. For comparison, cementitious pastes were prepared with neat SB microparticles at 0.11% wt% (SB/0.1), 0.24 wt% (SB/0.2), and 0.55wt% (SB/0.5). For the tensile strength tests and scanning electron microscopy only the REF (0 wt%), SB/PDA/Cr/0.5, and SB/0.5 samples were prepared (Table 1). The samples used in the leaching assays dried in the air (~ 24 °C and ~ 70% air humidity) for 28 days. The samples submitted to the tensile strength were previously cured in water for 28 days.

2.6.1. Mechanical tests and morphology of the fracture surface

Mechanical tests were performed for 45 cubic (10 mm – cubic size specimens) samples of the same type, using a point load test - linear variable displacement transducers (PLT-LVDT) (ASTM, 2008). The compression load was applied by hemispheres of tungsten in quasi-static condition, with a load rate of 0.02 mm.min^{-1} in two parallel faces of the flat faces of cubic samples. The assay was performed in a universal Instron machine (Model 5569). The morphology of the fracture surface was gold-sputtered and analyzed using a Jeol Neoscope microscope JCM 5000 operating at a voltage of 10 kV. The process of production of the cubes is depicted in the **Supplementary Material SM7.**

2.6.2. Incorporation of spent adsorbent into cement paste and leaching assays

In order to evaluate the leaching of Cr(VI) ions from the dry cement samples, samples of each composition (SB/PDA/Cr/0.1, SB/PDA/Cr/0.2, and SB/PDA/Cr/0.5) were immersed in distilled water (pH 5.5), simulating the protocol described elsewhere (EA, NEN 7375., 2004). The mass of distilled water was equivalent to three-fold the mass of each sample: this ratio was chosen because the protocol indicates water content from 2 to 5 times the mass of solid material. Aliquots of the aqueous medium that were in contact with the cementitious samples were withdrawn after 6 h, 1 day, 2 days and 6 h, 4 days, 9 days, 16 days, 36 days, and 64 days, and the presence of Cr(VI) in the leachate was analyzed by ICP OES (**Supplementary Material SM8**).

2.7. Statistical analysis

Experimental data were statistically analyzed by the software Minitab 17. One-way ANOVA was used to evaluate whether the differences among the groups were statistically significant. The test of multiple comparisons for unbalanced data was based on the Tukey-Kramer algorithm. This analysis was applied to assess the statistically significance the variation of the load rupture property after the addition of the spent adsorbent to the cement paste. Analyzed values that presented statistical difference were coded with the same letter, whereas those that presented no statistical difference were coded with the same letter (**Supplementary Material SM9**).

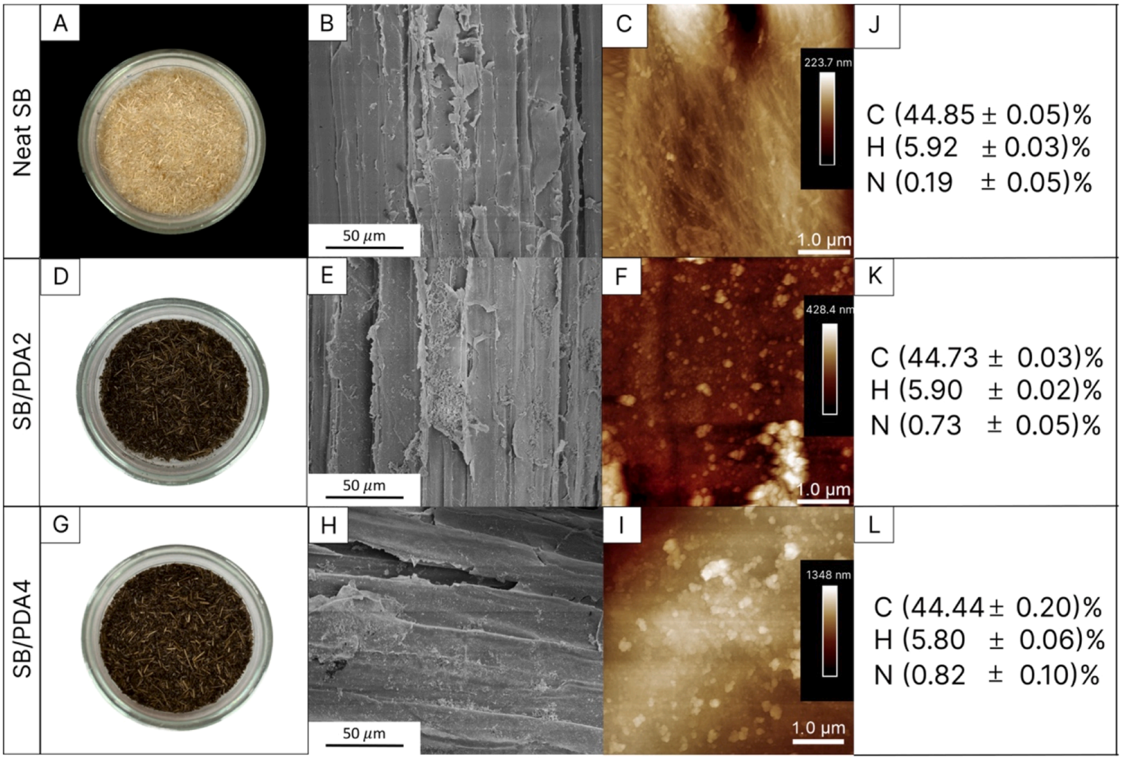

Fig. 1. Digital photographs (A), (D), (G), scanning electron micrographs (B), (E), (H) and topographic AFM images (C), (F), (I) of the surface of neat SB, SB/PDA2, SB/PDA4 samples, respectively. Elemental analyses (CHN) of neat SB (J), SB/PDA2 (K) and SB/PDA4 (L) samples.

3. Results and discussion

3.1. Characterization of the adsorbents

Fig. 1 shows photographs, SEM images and AFM images of the neat SB, SB/PDA2 and SB/PDA4 particles. After the reaction with PDA, the SB particles (Fig. 1**A**) turned dark (Fig. 1**D and G**), evidencing the successful deposition of PDA on them. The AFM image of neat SB surface showed the typical fibers (Fig. 1**C**). SEM and AFM images of SB/PDA2 and SB/PDA4 indicated the presence of small particles and aggregates on surface of the SB particles, which were attributed to the adhesion of PDA onto the SB surface. However, no morphological distinction could be made between SB/PDA2 (Fig. 1**E and F**) and SB/PDA4 (Fig. 1**H and I**). The mean roughness values (Ra) determined from the AFM images of SB, SB/PDA2, and SB/PDA4 amounted to 26 nm, 35 nm, and 35 nm, respectively, indicating that the deposition of PDA increased the surface roughness of SB surface. The deposition of PDA on cellulose nanocrystals (CNCs) also led to the formation of PDA nanoparticles distributed along the CNC surface (Dong et al., 2019). The CHN elemental analyses (Fig. 1**J–L**) revealed that the content of N increased from 0.19% (neat SB) to 0.73% (SB/PDA2) and 0.82% (SB/PDA4), confirming the successful coating of SB particles by PDA. Noteworthy, the increase of DA concentration from 2 g.L^{-1} to 4 g.L^{-1} did not increase the N content on SB particles at the same proportion. The mean surface area values determined for neat SB and SB/PDA4 were similar and amounted to 0.8 ± 0.1 m^2.g^{-1}. Typical N_2 adsorption/desorption isotherms (Type II) and the corresponding pore distribution determined by the BJH method indicated a wide distribution of pore sizes in the mesopore range (**Supplementary Material SM10)**.

FTIR spectra obtained for SB, SB/PDA2, and SB/PDA4 are provided as **Supplementary Material SM11**. PDA is composed of different products resulting from the oxidation of dopamine (dopamine quinone, 5,6-dihydroxyindole, catecholamine-based products) (Chen et al., 2017). The characteristic bands of PDA overlapped those of SB. All spectra presented an intense broad band from 2997 cm^{-1} to 3693 cm^{-1}, attributed to the axial deformation of O–H, present in the cellulose, hemicellulose, and lignin contents of the biomass (Furtado et al., 2020; Novaes et al., 2022; Silverstein and Bassler, 1962). The bands assigned to carboxyl groups (1728 cm^{-1}), carboxylate (1632 cm^{-1}) and the lignin aromatic ring (1603 cm^{-1} and 1372 cm^{-1}), were also observed. The bands in the wavenumber range from 1000 to 1350 cm^{-1} represented the overlapping signals of the C–C and C–O groups, with angular deformation stretching of carboxylic acids C–O of axial deformation vibration, corresponding to the cellulose composition and vibrations of axial deformation of symmetrical and asymmetric C–O–C strain of glycosidic rings present in the composition of the biomass. PDA characteristic bands at 1288 cm^{-1}, assigned to the catecholic C–OH (stretching) band, and at 1424 cm^{-1} assigned to O—H bending and C=C stretching of PDA are overlapped by the characteristic bands of SB. The bands at 664 cm^{-1} are related to bending modes of aromatic compounds, confirming the presence of lignin structure in the sugarcane bagasse.

3.2. Adsorption tests in the batch mode

3.2.1. Adsorption kinetics

Preliminary experiments showed that the removal capacity of Cr(VI) ions by neat SB was very low (2.85% for Cr(VI) at 100 mg.L^{-1}), in agreement with previous reports Meneses et al., 2022). For this reason, the experiments with neat SB were discontinued (**Supplementary Material SM12**). The experimental data did not fit to the pseudo-first order, pseudo-second order, mixed-order, and pseudo-nth-order models (**Supplementary Material SM13**), but they fitted to the Elovich and Weber-Morris (intraparticle diffusion), described by the linearized Eqs. (3) and ((4), respectively (Wang and Guo, 2020):

$$q_t = \frac{1}{\beta}\,(\ln(1+\alpha\beta t) \qquad (3)$$

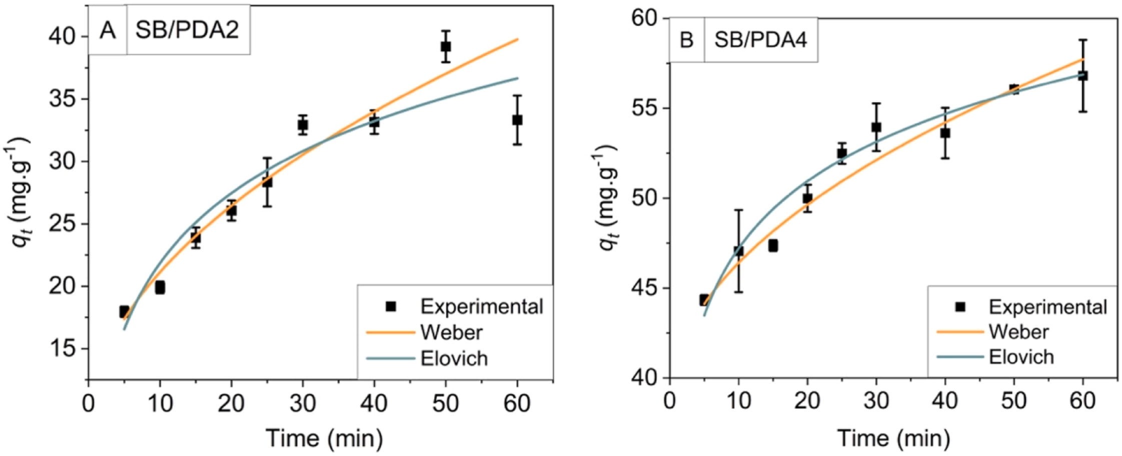

Fig. 2. . Adsorption kinetics of Cr(VI) ions at 150 mg.L^{-1} on SB/PDA2 (A) and SB/PDA2 (B), at (22 ± 1) °C and pH 2. The solution volume and adsorbent mass were 4 mL and 10 mg, respectively. The blue and orange lines represent non-linear fittings to the Elovich and Weber-Morris models, respectively.

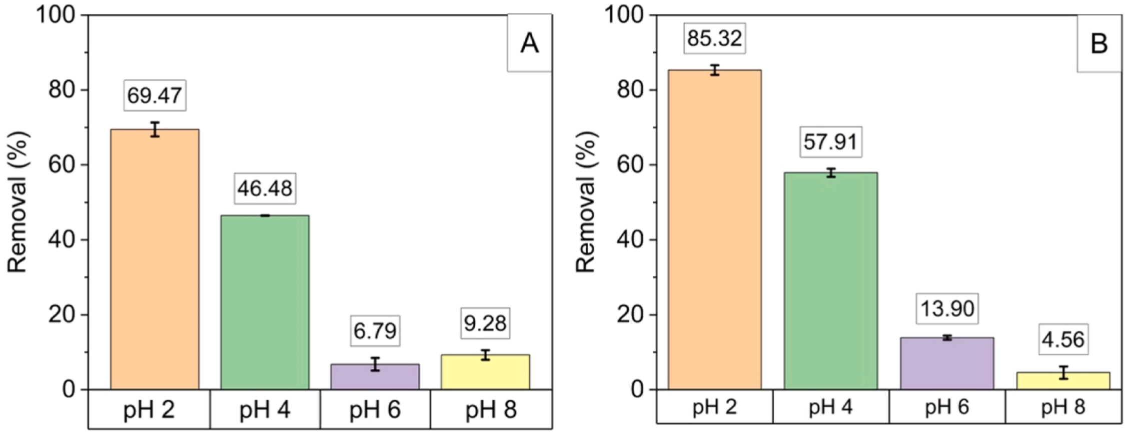

Fig. 3. Effect of the medium pH on the removal capacity of SB/PDA2 (A) and SB/PDA4 (B), towards Cr(VI) ions at $C_0 = 150$ mg.L^{-1}, 22 ± 1 °C, and 1 h of contact. The solution volume and adsorbent mass were 4 mL and 10 mg, respectively.

Where q_t (mg.g^{-1}) is the adsorbed amount at time t, β is the number of sites available for adsorption, and α is the initial adsorption rate (mg.g. min^{-1}).

$$q_t = k_{id} t^{\frac{1}{2}} \tag{4}$$

Where k_{id} is the intraparticle diffusion rate (mg.g^{-1}.min$^{-1/2}$).

Fig. 2**A** and **B** show the adsorption kinetics of Cr(VI) ions at 150 mg. L^{-1} (pH 2), on SB/PDA2 and SB/PDA4, respectively. After 60 min, the q_t values did not increase significantly.

The non-linear fitting parameters in the **Supplementary Material SM14** showed that the experimental data fitted better to the Weber-Morris model than to the Elovich model. The Weber-Morris model has been widely applied for the analysis of mass transfer from solution to the solid-liquid interface. For the adsorption time of 60 min, the calculated q_t values observed for Cr(VI) ions (150 mg.L^{-1}) on SB/PDA2 and SB/PDA4 were ~ 40 mg.g^{-1} and ~ 58 mg.g^{-1}, respectively, indicating that the higher mount of PDA on SB/PDA4 increased the affinity for Cr(VI) ions. The intraparticle diffusion rate (k_{id}) values determined for Cr(VI) on SB/PDA2 and SB/PDA4 amounted to 3.977 mg.g^{-1}.min$^{-1/2}$ and 2.504 mg.g^{-1}.min$^{-1/2}$, respectively. These trends indicate that the slowest transport rate of Cr(VI) ions from the solution to the surface of SB/PDA4 allowed a more efficient occupation of the adsorbing sites, avoiding electrostatic repulsion among the arriving chromate ions and the already adsorbed chromate ions. Dong and coworkers (Dong et al., 2019) reported the k_{id} and q_t values for Cr(VI) at 200 mg.L^{-1}, pH 3, on PDA coated cellulose nanocrystals (CNC/PDA) for 24 h adsorption, as 2.328 mg.g^{-1}.min$^{-1/2}$ and ~ 58.87 mg.g^{-1}, respectively, which are on the same order of magnitude to those reported here.

3.2.2. The effect of the medium pH on the removal capacity of SB/PDA2 and SB/PDA4 towards Cr(VI) ions

Hexavalent chromium might exist in six forms of oxyanions in aqueous solutions, including $HCr_2O_7^-$, $Cr_3O_{10}^{2-}$, $H_2Cr_2O_4$, $HCrO_4^-$, $Cr_2O_7^{2-}$ and CrO_4^{2-}, which depend on the pH of the aqueous solution and the concentration of hexavalent chromium (Jin et al., 2018). For instance, at pH between 1 and 6, the dominant form of Cr(VI) is $Cr_2O_7^{2-}$ and $HCrO_4^-$, whereas at pH > 6, the dominant form of Cr(VI) is CrO_4^{2-}. Fig. 3 shows that the removal capacity of SB/PDA2 and SB/PDA4 decreased drastically when the pH was less than 4. The point of zero charge (PZC) values determined for SB/PDA2 and SB/PDA4 were similar and amounted to ~ 3 (**Supplementary Material SM15**). At pH lower than 3 the carboxylic acid groups are protonated avoiding electrostatic repulsion between carboxylate and chromate ions, whereas the amino groups stemming from PDA are protonated (Ding et al., 2014), favoring the electrostatic interaction between the chromium oxyanions and the adsorbent. At pH higher than 4, the carboxylic acid groups are deprotonated, repelling the Cr(VI) anions. Based on these results all adsorption isotherms were performed at pH 2.

It is important to mention two real situations where the wastewater

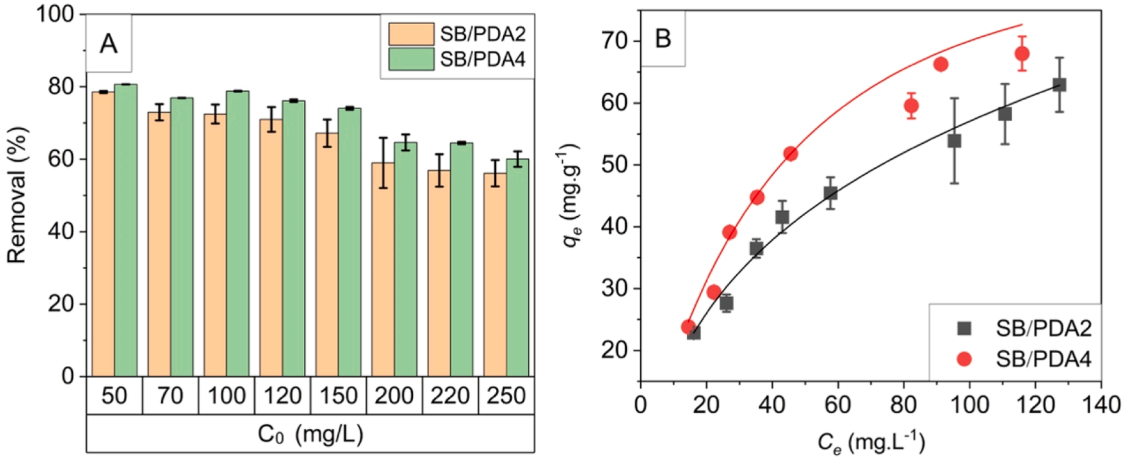

Fig. 4. (A) Mean values of removal capacity (%) of Cr(VI) ions on SB/PDA2 and SB/PDA4; the initial concentration (C_0) ranged from 50 to 250 mg.L^{-1}. (B) Adsorption isotherms of Cr(VI) ions on SB/PDA2 and SB/PDA4. The black and red lines represent non-linear fittings to the Khan adsorption model. All experiments were carried out at pH = 2, 22 ± 1 °C, and 1 h of adsorption. For all experiments, the solution volume and adsorbent mass were 4 mL and 10 mg, respectively.

Table 2

Khan nonlinear fitting parameters for the adsorption of Cr(VI) on different adsorbents. a_k, b_k, and q_{max} stand for Khan isotherm model exponent, Khan constant, and maximum adsorption capacity, respectively.

Adsorbent		q_{max} (mg.g^{-1})	b_k (L.mg^{-1})	a_k (L.g^{-1})	R^2	
*SB/PDA2		30.62	0.0801	0.663	0.9863	This work
*SB/PDA4		138.66	0.0156	1.199	0.9822	
Chemically modified	Date pits	59.19	0.02	1.06	0.93	Mangwandi et al. (2020)
	Olive stone	3.06	0.41	23.62	0.89	
Durian rind	raw	124.5	0.011	0.868	0.977	Sulistiyo et al. (2022)
	Extracted cellulose	154.2	0.013	1.047	0.991	
	Activated carbon	223.3	0.095	0.086	0.999	
Marine brown algae modified with	Epichlorohydrin	26.09	0.0455	1.3202	0.990	Basha and Murthy (2007)
	Potassium permanganate	23.86	0.0493	1.2774	0.982	
	Washed with distilled water	21.69	0.0472	1.3078	0.997	
Lignin		29.1	0.11	−0.55	0.94	Albadarin et al. (2011)
Natural Clay		10.83	0.179	0.942	0.999	Khalfa et al. (2016)
Acid-Activated clay		19.69	0.572	1.024	0.9916	

[*] Experimental conditions: biosorbent dose 2.5 g.L^{-1}; contact time 1 h at pH 2 and 22 °C.

might be acid. The first one is the tannery wastewater that might present pH as low as 3 (Bingül et al., 2022; Chowdhury et al., 2015), and the second one is the waste from undergraduate laboratory, which is a complex sample with many metal ions at pH 1 because it contains solutions discarded by the students after practical classes of General Chemistry and Analytical Chemistry (Furtado et al., 2022). In general, low pH values avoid the possible metal ion precipitation as metal hydroxides. In both situations, it is environmentally relevant to remove Cr (VI) ions before discarding the wastewater.

3.2.3. *Adsorption isotherms of Cr(VI) on SB/PDA2 and SB/PDA4*

Fig. 4**A** and **B** show the removal capacity and the adsorption isotherms determined for Cr(VI) on SB/PDA2 and SB/PDA4, respectively, at (22 ± 1) °C and pH 2. In general, Cr(VI) showed significantly ($p < 0.05$) higher affinity for the SB/PDA4 adsorbents than for the SB/PDA2 adsorbents. This indicated that increasing the PDA on the surface created more adsorbing sites (such as o-quinone, carboxy, amino, imine, phenol, and N—H groups), favoring the affinity of Cr(VI) for the adsorbents.

Among the most common models (Ayawei et al., 2017), eight adsorption isotherm models were applied to fit the experimental adsorption data, as presented by **Supplementary Material SM16**. The experimental adsorption isotherms of Cr(VI) on SB/PDA2 and SB/PDA4 fitted well only the Redlich-Peterson and Khan models. However, the fitting parameter *g* of the Redlich-Peterson model was larger than 1 in the case of SB/PDA4 sample, which is not predicted by the model. For this reason, only the Khan model (Khan et al., 1997) was considered; its isotherm equation is:

$$q_e = \frac{q_{max} b_k C_e}{(1 + \ b_k C_e)^{a_k}} \tag{5}$$

Where a_k is Khan isotherm model exponent, b_k is Khan isotherm model constant, and q_{max} (mg.g^{-1}) is Khan isotherm maximum adsorption capacity. Khan isotherm equation combines features of the Langmuir and Freundlich isotherm equations (Khan et al., 1997).

Table 2 shows the Khan nonlinear fitting parameters for the adsorption of Cr(VI) on SB/PDA2 and SB/PDA4 and on other biobased adsorbents, for comparison. The q_{max} values determined for Cr(VI) on SB/PDA2 and SB/PDA4 were 30.62 mg.g^{-1} and 138.66 mg.g^{-1}, respectively, indicating that SB/PDA4 has more adsorbing sites than SB/PDA2. In comparison to other adsorbents (Table 2), only Durian rind based adsorbents were better than SB/PDA4. The adsorption of Cr(VI) on lignin (Albadarin et al., 2011) and marine brown algae modified with epichlorohydrin (Basha and Murthy, 2007) led to q_{max} values of 29.1 mg.g^{-1} and 26.09 mg.g^{-1}, respectively, evidenced that coating SB particles with PDA at 4 g.L^{-1} increased considerably the adsorption efficiency.

3.2.4. *The adsorption mechanism of Cr(VI) on SB/PDA2 and SB/PDA4*

The adsorption constant (K_{ads}) can be estimated by the ratio between the adsorbate on the solid phase (q_e) and the adsorbate in the liquid phase (C_e) under equilibrium (Do, 1998). The van't Hoff equation allows

Table 3

. Adsorption free energy change (ΔG_{ads}, kJ mol^{-1}), enthalpy change (ΔH_{ads}, kJ mol^{-1}), and entropy change (ΔS_{ads}, J mol^{-1}K^{-1}) determined for the adsorption of Cr (VI) on SB/PDA2 and SB/PDA4 and on other PDA-based adsorbents.

Adsorbent	T (K)	Thermodynamic Parameters			
		ΔG_{ads} (kJ mol^{-1})	ΔH_{ads} (kJ mol^{-1})	ΔS_{ads} (J mol^{-1}K^{-1})	
SB/PDA2	299.3	−12.22	5.73	60.86	This work
	304.6	−12.53			
	309.4	−12.82			
SB/PDA4	299.3	−8.80	11.12	66.57	
	304.6	−9.15			
	309.4	−9.47			
PDA functionalized attapulgite supported nano sized zero-valent iron composite	293	−24.08	30.22	185.61	Ma et al. (2022)
	298	−24.50			
	308	−25.90			
PDA microspheres	293	−2.45	17.37	0.066	Zhang et al. (2018)
	313	−3.40			
	333	−5.17			
Electrospun polyethersulfone/ PDA nanofibers	293	−6.41	24.11	104.17	Wei et al. (2021)
	298	−6.93			
	308	−7.97			
Mesoporous PDA/TiO_2 composite nanospheres	298	−2.43	35.41	127.04	Li et al. (2019)
	308	−3.70			
	318	−4.97			
Fe(III)-PDA complex modified Mg/Al layered double hydroxide	298.2	−5.196	39.48	149.71	Chen et al. (2022a)
	303.2	−5.835			
	308.2	−6.696			
Core–shell magnetic PDA nanocomposite	298	−23.53	33.83	0.196	Yang et al. (2021)
	308	−26.24			
	318	−28.47			
Porous PDA	298	−4.405	24.621	0.096	Xiang et al. (2020)
	313	−5.268			
	333	−6.424			
Magnetic hollow composites Fe_3O_4@A/PDA	298	−0.344	14.807	50.728	Li et al. (2017)
	308	−0.756			
	318	−1.354			

estimating the adsorption enthalpy change (ΔH_{ads}, J mol^{-1}) and entropy change (ΔS_{ads}, J mol^{-1}K^{-1}) considering that ΔH_{ads} does not depend on the temperature, over the temperature range investigated (Chang, 2000):

$$lnK_{ads} = -\frac{\Delta H_{ads}}{R} \times \frac{1}{T} + \frac{\Delta S_{ads}}{R} \tag{6}$$

The ΔH_{ads} and ΔS_{ads} values were calculated from the slope and intercept of the plot of ln K_{ads} versus 1.T^{-1}, respectively. R is the universal gas constant (8.314 J mol^{-1} K^{-1}), T is the temperature (K). The value of ΔG_{ads} was obtained by (Chang, 2000):

$$\Delta G = \Delta H - T\Delta S \tag{7}$$

Supplementary Material SM17 provides the dependence of ln K_{ads} as a function of T^{-1} for the adsorption of Cr(VI) ions on SB/PDA2 and SB/PDA4 at pH 2. Table 3 shows the adsorption free energy change (ΔG_{ads}, kJ mol^{-1}), enthalpy change (ΔH_{ads}, kJ mol^{-1}), and entropy change (ΔS_{ads}, J mol^{-1}K^{-1}) determined for the adsorption of Cr (VI) on SB/PDA2 and SB/PDA4 and on other PDA-based adsorbents, for comparison. The negative values of ΔG_{ads} (~ -12 kJ.mol^{-1} and ~ -9 kJ. mol^{-1} for the adsorption of Cr(VI) on SB/PDA2 and SB/PDA4, respectively), indicated a spontaneous adsorption process (Chang, 2000). The positive values of ΔH_{ads} revealed that the adsorption process has an endothermic nature, which might be due to ion-dipole interactions (Elanchezhiyan et al., 2016) or electrostatic interactions (Xu et al., 2023). The positive values of ΔS_{ads} suggested an entropic gain due to the release of counter-ions and/or water molecules caused by the adsorption process (Nithya et al., 2016). Since TΔS_{ads} values surpassed the ΔH_{ads} values, it is plausible to conclude that the adsorption of Cr(VI) on the SB/PDA2 or SB/PDA is entropically driven. In comparison to other PDA based adsorbents (Xiang et al., 2020; Zhang et al., 2018), all of them presented endothermic adsorption process, but the ΔS_{ads} values varied by some orders of magnitude. For instance, when porous PDA or PDA microspheres were used as adsorbents, the ΔS_{ads} values were very small, indicating that the adsorption of Cr(VI) on them did not promote the release of counter-ions (H^+ or OH^- from water dissociation) or water molecules.

XPS analyses were carried out on SB microparticles, SB/PDA2 and SB/PDA4 adsorbents before and after the adsorption of Cr(VI) to gain more insight into the adsorption mechanism. As a control, the standard reagent $K_2Cr_2O_7$ was also analyzed, and a comparison between the Cr 2p XPS spectra before and after the adsorption process is shown in the **Supplementary Material SM18.** Fig. 5 shows the high-resolution XPS spectra of C 1 s (A, C, F, J and N), O 1 s (B, D, G, L, and O), N 1 s (E, H, M, and P), and Cr 2p (I and Q), which were fitted using Gaussian function (CasaXPS software). The dotted lines represent the experimental data, and the dashed lines represent the fitted data. The area (%), and binding energy peak position (eV) values were provided as **Supplementary Material SM19.**

The C1s spectra of SB/PDA2 and SB/PDA4 before and after Cr(VI) adsorption could be deconvoluted into 4 peaks C—C/C=C (284.0 eV), C—OH (286.1 eV), C=O (287.3 eV), and O—C=O (288.9 eV), which are typical of the oxidation products of dopamine (Liebscher et al., 2013). SB also presented the peaks corresponding to C—C/C=C, C—OH, and C=O, which are typical of lignocellulosic materials (Furtado et al., 2022).

The O 1 s spectra of SB/PDA2 and SB/PDA4 presented peaks at 533.0 and 531 eV that were assigned to C—O-H, and C=O, respectively (Luo et al., 2022). After the adsorption of Cr(VI) on SB/PDA the peaks related to C—O-H shifted −0.88 eV and −1.29 eV, respectively and SB/PDA4, the peaks related to C=O shifted +0.35 and +1.16 eV, respectively. Such shifts suggest the possible formation of C—O-Cr, C=O—Cr, and O—Cr-O bonds (Chen et al., 2022b). Comparing the SB spectrum with those of SB/PDA2 or SB/PDA4, it can be perceived the appearance of C=O bond, which can be related to the dopamine self-polymerization to form the benzoquinone structure (Dreyer et al., 2012). After the adsorption of Cr (VI) ions, the peak area related to (C=O) increased significantly, part of catechol groups (C—OH) has been probably oxidized to quinone groups confirming the auto-oxidation of dopamine (Liebscher et al., 2013).

The N 1 s spectra of SB/PDA2 and SB/PDA4 were decomposed into 4 peaks at 402.7, 401, 400, and 399.4 eV, assigned to -NH_3^+/-NH_2^+/-NH^+, -NH_2, -NH-, and =*N*-, respectively, attesting the presence of PDA on SB microparticles (Zhu et al., 2017). After the adsorption of Cr(VI), the peak areas assigned to -NH_3^+ and -NH_2^+decreased significantly, indicating possible electrostatic interactions between them and chromate ions (Zhang et al., 2022). Only after the adsorption of Cr(VI) on SB/PDA4 significant shifts in the peak positions could be observed; the peaks corresponding to -NH_3^+ and -NH_2 shifted −2.22 and −0.60 eV, respectively, probably due to the presence of chromate ions.

The Cr 2p spectrum of $K_2Cr_2O_7$ sample (**Supplementary Material SM18**) has two peaks, Cr $2p_{3/2}$ (580.13 eV) and Cr $2p_{1/2}$ (589.32 eV), respectively; after the adsorption on SB/PDA2 or SB/PDA4, they shifted to −2.88 eV and −2.22 eV (Shokouhfar et al., 2018). Such energy shifts can be attributed to the strong affinity between the SB/PDA adsorbents with the Cr(VI) ions. The peaks located at ≈ 576 eV and ≈ 586 eV can be attributed to Cr(III) (Shokouhfar et al., 2018). The presence of Cr(III) indicated that part of the Cr(VI) ions were reduced to Cr(III) ions on the adsorbent surface (Verma et al., 2021). Cellulose hemiacetal reducing ends and PDA catechol groups probably caused the reduction of Cr(VI) to Cr(III), and consequently underwent oxidation. This hypothesis is supported by the increase of the peak areas of C 1 s (O—C=O) and O 1 s (C=O) after the Cr(VI) adsorption (**Supplementary Material SM19**). The adsorption and subsequent reduction of Cr(VI) to Cr(III) was also observed on sulfidemodified nanoscale zerovalent iron (Lv et al., 2019).

From the XPS survey spectra **(Supplementary Material SM20)** the chemical composition and the elemental ratios C/O and N/C were

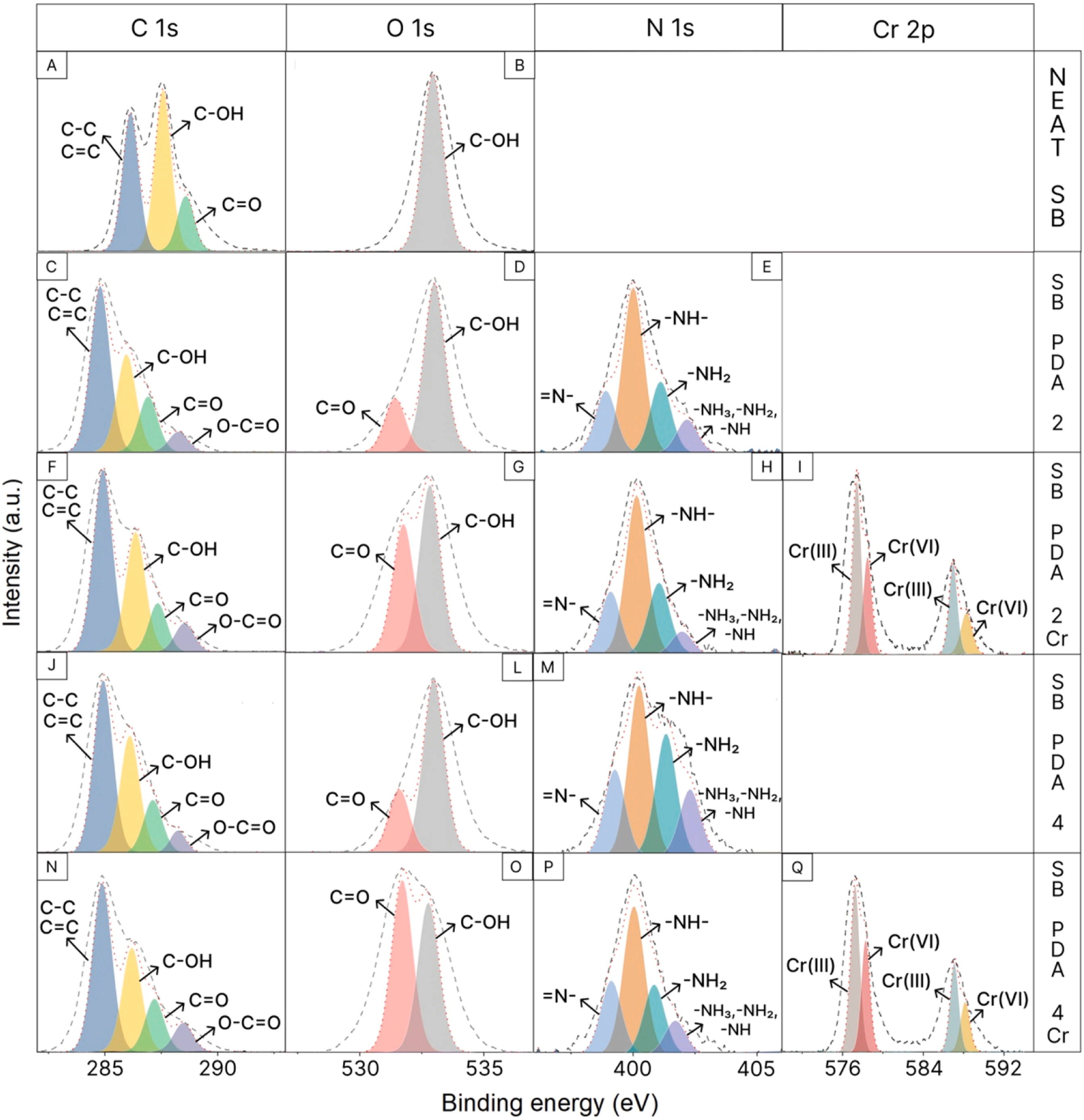

Fig. 5. . High resolution XPS spectra of C 1 s (A, C, F, J, and N), O 1 s (B, D, G, L, and O), N 1 s (E, H, M, and P) and Cr 2p (I and Q) obtained for SB microparticles, SB/PDA2 and SB/PDA4 before and after Cr(VI) adsorption (SB/PDA2Cr and SB/PDA4Cr). Dashed and dotted represents the experimental bands and the fitted bands, respectively.

calculated for SB, SB/PDA2 and SB/PDA4 before and after the adsorption of Cr(VI) ions (Table 4). In comparison to neat SB, SB/PDA2 and SB/PDA4 presented increased C/O ratio from 2.34 to 3.77 and 3.74, respectively, and N appeared at 4.42% and 5.14%, respectively. These findings evidence the presence of PDA on SB microparticles and show an increase of N content, when the dopamine solution was increased from 2 $g.L^{-1}$ to 4 $g.L^{-1}$, in agreement with the elemental analysis (CHN) presented in Fig. 1**K** and **L**. After the adsorption of Cr(VI), the C/O and N/C elemental ratios decreased, indicating that the catechol, quinone and amine groups interacted with the Cr(VI) ions. Furthermore, the content of Cr on SB/PDA4 was considerably higher than on SB/PDA2, in agreement with the corresponding q_{max} values (Table 2), and the oxygen content increased due to the adsorption of the oxyanions (($HCrO_4^-$, CrO_4^-) (Wan et al., 2021).

Based on the analysis of the XPS spectra and thermodynamic parameters, the adsorption mechanism of Cr(VI) ions on SB/PDA2 and SB/PDA4 adsorbents can be described as follows: (1) metal-ligand complexation through functional groups of PDA (amino, catechol, quinone, carboxyl) (Zhang et al., 2018); (2) electrostatic interaction between positively charged sites available at pH 2 ($-NH_3^+$) and chromate anions; and (3) the reduction of Cr(VI) to Cr(III) ions promoted by active groups on the surface (hemiacetal, catechol) that undergo oxidation

Table 4
Percentual fraction of C, O, N, and Cr elements determined for SB, SB/PDA2, SB/PDA4, SB/PDA2 after the adsorption of Cr(VI) at 150 mg.L^{-1} (SB/PDA2Cr), and SB/PDA4 after the adsorption of Cr(VI) at 150 mg.L^{-1} (SB/PDA4Cr), and the respective C/O and N/C ratios.

Composition	Fraction (%)				Ratio	
	C	O	N	Cr	C/O	N/C
SB	70.02	29.98	–	–	2.34	–
SB/PDA2	75.54	20.04	4.42	–	3.77	0.22
SB/PDA2Cr	65.19	29.53	2.92	2.35	2.21	0.10
SB/PDA4	74.83	20.03	5.14	–	3.74	0.26
SB/PDA4Cr	59.80	33.44	2.65	4.11	1.79	0.08

(Luo et al., 2022).

3.3. Fixed-bed column studies

The studies of batch adsorption are important because they allow understanding how the adsorbate interacts with the substrate under equilibrium conditions. However, for practical purposes, where large amounts of wastewater should be treated, column adsorption studies are more appropriate because the column operational conditions can be optimized in order to achieve the highest efficiency. Fig. 6**A** and **B** show the breakthrough curves obtained online by the column coupling to the ICP-OES, for Cr(VI) on SB/PDA2 and SB/PDA4, respectively. The initial adsorbate concentration C_0 (20, 75, and 150 mg.L^{-1}), and the mass of adsorbent *m* (50, 100, and 500 mg) were varied. Experimental data were fitted to the nonlinear Thomas model to understand how the amount of the adsorbent in the column (*m*), the initial adsorbate concentration (C_0) and the flow rate (ν) of the solution through the column affect the adsorption capacity (q_0) (Thomas, 1944):

$$\frac{C_t}{C_0}=\frac{1}{1+exp\left[\frac{K_{Th}}{\nu}q_0m-K_{Th}C_0t\right]} \tag{8}$$

where C_t is the concentration of effluent at any time and the corresponding time (t), and K_{th} is the Thomas rate constant (mL min^{-1} mg^{-1}). The model is suitable for predicting adsorption when ignoring internal and external diffusion resistances (Thomas, 1944). The fitting procedure was done with OriginPro 2021 software, applying a non-linear fitting called slogistic1, which is equivalent to Thomas model (Thomas, 1944), as described in the **Supplementary Material SM21.** Table 5 shows the experimental conditions applied for the breakthrough curves of Cr(VI) ions on SB/PDA2 and SB/PDA4 and the corresponding non-linear fitting parameters of Thomas model, K_{TH} (L.mg^{-1} min^{-1}) and q_0 (mg.g^{-1}).

Preliminary, the flow rate was varied from 0.8 to 1.5 mL.min^{-1}, for Cr(VI) ($C_0 = 75$ mg.L^{-1}) on SB/PDA4 ($m = 100$ mg). Although at 0.8 mL. min^{-1} the q_0 value was considerably higher (72.94 mg.g^{-1}) than at 1.5 mL.min^{-1} (52.97 mg.g^{-1}), the column saturation ($C_t/C_0 = 0.9$) took 5 five h, as shown in the **Supplementary Material SM22**. Considering the large number of experiments, the slowest flow rate would significantly extend the overall period of the experiments. For this reason, all

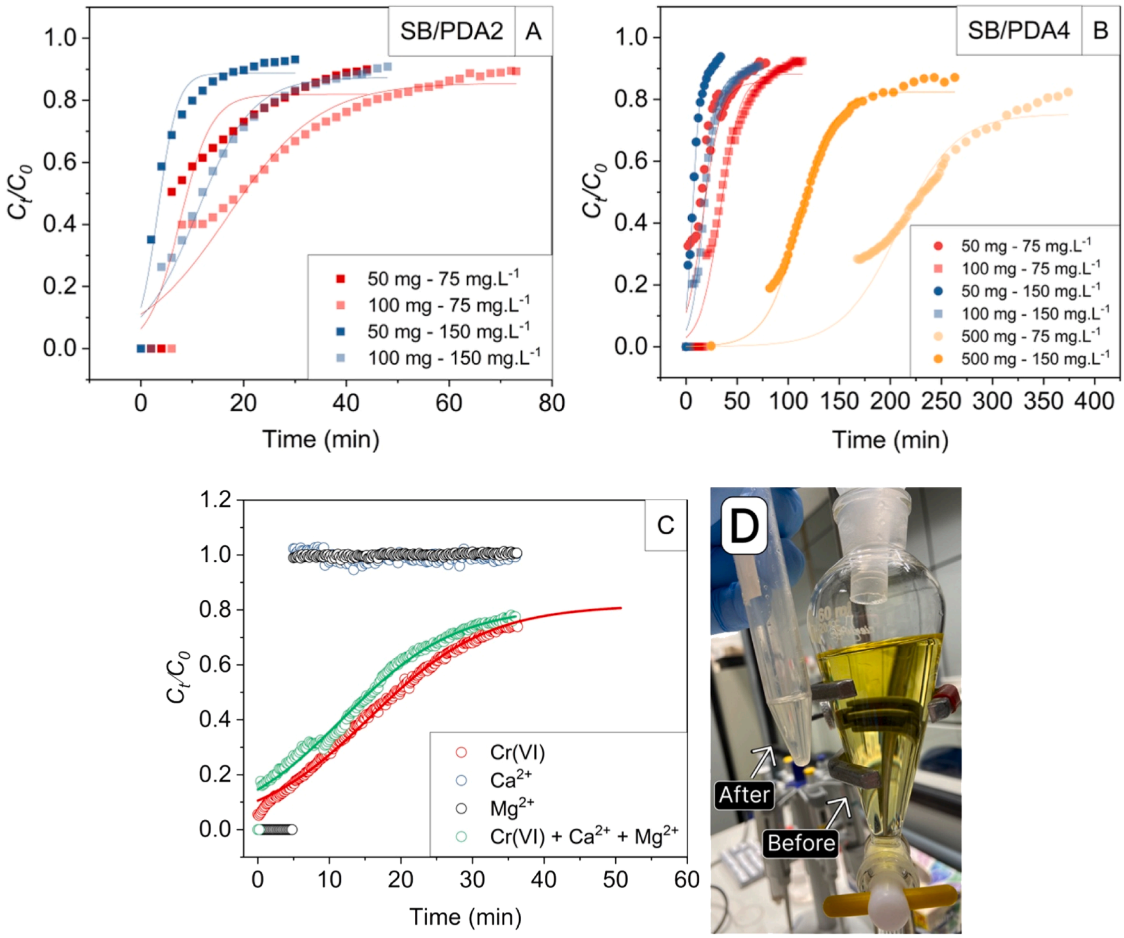

Fig. 6. Breakthrough curves for Cr(VI) ions on (A) SB/PDA2 and (B) SB/PDA4 at pH 2 and $\nu = 1.5$ mL.min^{-1}, for different adsorbent mass (*m*) and initial Cr(VI) concentration (C_0) values. (C) Breakthrough curves for Cr(VI) ions on SB/PDA4 ($m = 50$ mg) at $C_0 = 20$ mg.L^{-1} in the absence (red symbols) and in the presence of Ca^{2+} and Mg^{2+} ions (green symbols), in the presence of the Ca^{2+} and Mg^{2+} ions (5 mg.L^{-1} each), and $\nu = 3$ mL.min^{-1}. The Ca^{2+} and Mg^{2+} ions are represented by blue and black symbols, respectively. The solid lines are the non-linear fittings to Thomas model. (D) Photograph of Cr(VI) solution at $C_0 = 150$ mg.L^{-1} before and after passing through the column.

Table 5

Experimental conditions applied for the breakthrough curves of Cr(VI) ions on SB/PDA2, SB/PDA4, and other bioadsorbents: C_0, ν, and m_{ads} stand for inlet initial concentration (mg.L^{-1}), flow rate (mL.min^{-1}), and mass of adsorbent (g), respectively. Fitting parameters of the Thomas model: K_{TH} (L.mg^{-1} min^{-1}) and q_0 (mg.g^{-1}) stand for the rate constant and adsorption capacity, respectively.

	Experimental conditions				Fitting parameters				
	C_0 (mg.L^{-1})	ν (mL.min^{-1})	Z (cm)	*m* (mg)	K_{TH} (L.mg^{-1} min^{-1})	q_0 (mg.g^{-1})	R^2	χ^2	
SB/PDA2	75	1.5	0.45	50	7.9×10^{-3}	24.52	0.904	0.00846	This work
	75	1.5	0.9	100	2.6×10^{-3}	26.19	0.936	0.00496	
	150	1.5	0.45	50	11.9×10^{-3}	19.79	0.956	0.00328	
	150	1.5	0.9	100	43×10^{-3}	33.09	0.975	0.00202	
SB/PDA4	75	0.8	0.9	100	1×10^{-3}	72.94	0.983	0.00185	
	75	1.5	0.45	50	1×10^{-3}	38.47	0.953	0.00267	
	75	1.5	0.9	100	23×10^{-3}	52.97	0.976	0.00272	
	75	1.5	4.5	500	14×10^{-3}	69.36	0.990	0.00246	
	150	1.5	0.45	50	62×10^{-3}	37.33	0.981	0.00161	
	150	1.5	0.9	100	36×10^{-3}	50.76	0.988	0.00105	
	150	1.5	4.5	500	9×10^{-3}	141.70	0.963	0.00105	
SB/PDA4$^{(I)}$	20	3.0	0.45	50	31×10^{-3}	48.52	0.997	1.703×10^{-4}	
SB/PDA4$^{(II)}$	20	3.0	0.45	50	33×10^{-3}	37.20	0.988	4.819×10^{-4}	
SB/PDA4$^{(III)}$	75	1.5	0.9	100	0.024	2.63	0.986		
SB/PDA4$^{(IV)}$	75	1.5	0.9	100	0.017	31.69	0.961		
CMC/SB/CTAB	95	0.8	–	170	2.14×10^{-3}	6.17	0.994	–	Meneses et al. (2022)
Rice Husk	100	5	4.3	–	0.143×10^{-3}	50.69	0.984	–	Yakout et al. (2019)
	50	5	2.5	–	0.3416×10^{-3}	68.79	0.988	–	
Garden waste	6.5	9	3	–	63×10^{-3}	18.715	0.882	–	Erabeea et al. (2019)
	6.5	12	3	–	0.085×10^{-3}	15.534	0.993	–	
Magnetic pine cone	50	1	2.5	–	0.0005×10^{-4}	5.87	0.998	–	Pholosi et al. (2020)
	100	1	2.5	–	0.00025×10^{-4}	33.08	0.986	–	
Magnetite Impregnated Husk	100	5	3.2	–	1.8×10^{-4}	53.0	0.975	–	Srivastava et al. (2019)
	100	10	3.2	–	2.4×10^{-4}	50.06	0.925	–	
Walnut shell	15	10	5	–	7.21×10^{-1}	30.10	0.942	–	Yahya et al. (2020)
	20	10	5	–	4.55×10^{-1}	35.52	0.955	–	
Almond shell	25	2	2	–	4.897	4.768	0.999	–	Cruz-Olivares et al. (2022)
	25	2	4	–	4.991	5.156	0.998	–	
	25	2	6	–	5.129	5.528	0.999	–	

Legend: χ^2 = Chi-square, SB/PDA4$^{(I)}$ and SB/PDA4$^{(II)}$ = Cr(VI) solution without and with the addition of Ca^{2+} and Mg^{2+} ions (5 mg.L^{-1} each), respectively. SB/PDA4$^{(III)}$ and SB/PDA4$^{(IV)}$ = Cr(VI) solution prepared in freshwater at pH 7, and pH 2, respectively.

breakthrough curves were performed at 1.5 mL.min^{-1}. Generally, the slow flow rate increases the contact time between the adsorbate and the adsorbent, increasing the adsorption efficiency (Furtado et al., 2022; Meneses et al., 2022; Novaes et al., 2022; Sun et al., 2014).

Comparing the q_0 values (Table 5) determined for SB/PDA2 and SB/PDA4 under similar experimental conditions, all columns packed with SB/PDA4 adsorbed Cr(VI) more efficiently than those filled with SB/PDA2. This trend was the same observed for the q_{max} values in Table 2. In general, the increase of adsorbent mass (*m*) led to longer saturation time and higher q_0 values. For instance, for C_0 = 150 mg.L^{-1}, the increase of *m* from 50 mg to 500 mg of SB/PDA4 adsorbents enhanced the q_0 values from 37.33 mg.g^{-1} (*m* = 50 mg) to 141.70 mg.min^{-1} (*m* = 500 mg). An explanation to this fact is that the number of adsorption sites increases upon enhancing the adsorbent mass. Similar trends were reported by other researchers (Gizaw et al., 2022; Kumari and Dey, 2019). For a fixed mass of adsorbent, when C_0 values varied from 75 mg.L^{-1} to 150 mg.L^{-1}, the q_0 values decreased. This effect might be due to an increase of electrostatic repulsion between the already adsorbed ions and the arriving ions (Furtado et al., 2022).

Ca^{2+} and Mg^{2+} ions are commonly found in natural waters (Kumar et al., 2022). For this reason, they were added (5 mg.L^{-1}, each) to the initial solution of Cr(VI) ions C_0 = 20 mg.L^{-1} (Fig. 6**C**). The presence of Ca^{2+} and Mg^{2+} ions reduced the adsorption capacity of SB/PDA4 towards Cr(VI) from q_0 = 48.52 mg.g^{-1} to q_0 = 37.20 mg.g^{-1} (Table 5). The coexistence of other ions might hinder the adsorption of Cr(VI) and reduce the adsorption efficiency, as cations can not only bind to anionic chromate but they can also compete for adsorbent sites (Deng et al., 2022). However, Fig. 6**C** showed that after approximately 5 min both cations were eluated from the column, suggesting that they have low affinity for the adsorbent. Thus, the decrease of q_0 was probably due to electrostatic interactions between chromate and Ca^{2+} and Mg^{2+} ions; such screening effect would weaken the interactions between Cr(VI) and the adsorbent. Nevertheless, the SB/PDA4 adsorbents still displayed considerably high adsorption capacity for Cr(VI) even in the presence of the interfering ions. The photograph in Fig. 6**D** shows that after passing through the fixed-bed column the solution became colorless. The q_0 values presented in Table 5 show that the SB/PDA2 and SB/PDA4 adsorbents outperformed other waste-based adsorbents.

Supplementary Material SM23 shows the breakthrough curves obtained with Cr(VI) solutions (C_0 = 150 mg.L^{-1}) prepared with freshwater (pH 7). The column filled with SB/PDA4 (*m* = 100 mg) saturated (C_t/C_0 ~90%) after 28 min and yielded q_0 of 2.63 g.mg^{-1} (Table 5). Under the same conditions, the breakthrough curves obtained for Cr(VI) solutions (C_0 = 150 mg.L^{-1}) prepared with freshwater and adjusted to pH 2 took 2.5 h to saturate an led to q_0 of 31.69 mg.g^{-1} (Table 5). These findings agree with the batch adsorption experiments (Fig. 3) that showed very low removal% at pH higher than 4 due to electrostatic repulsion between the negatively charged surface and chromate ions. Furthermore, at pH 2 the possible presence of ions in the freshwater reduced the q_0 values from 52.97 mg.g^{-1} (MilliQ water) to q_0 of 31.69 mg.g^{-1} (freshwater), due to competitive adsorption and screening effects, as observed in the presence of Ca^{2+} and Mg^{2+} ions. The mean surface area of the SB/PDA4 measured after the adsorption process at pH 2 ($q_0 \sim$ 142 mg.g^{-1}) amounted to 1.1 ± 0.2 m^2.g^{-1}; there was no statistically significant difference between this value and that determined for SB/PDA4 before the adsorption (0.8 ± 0.1 m^2.g^{-1}).

3.4. Cementitious materials containing spent SB/PDA2 and SB/PDA4 adsorbents

The concentration of chromium element in the aqueous media that were in contact with cement pastes (SB/PDA/Cr/0.1, SB/PDA/Cr/0.2,

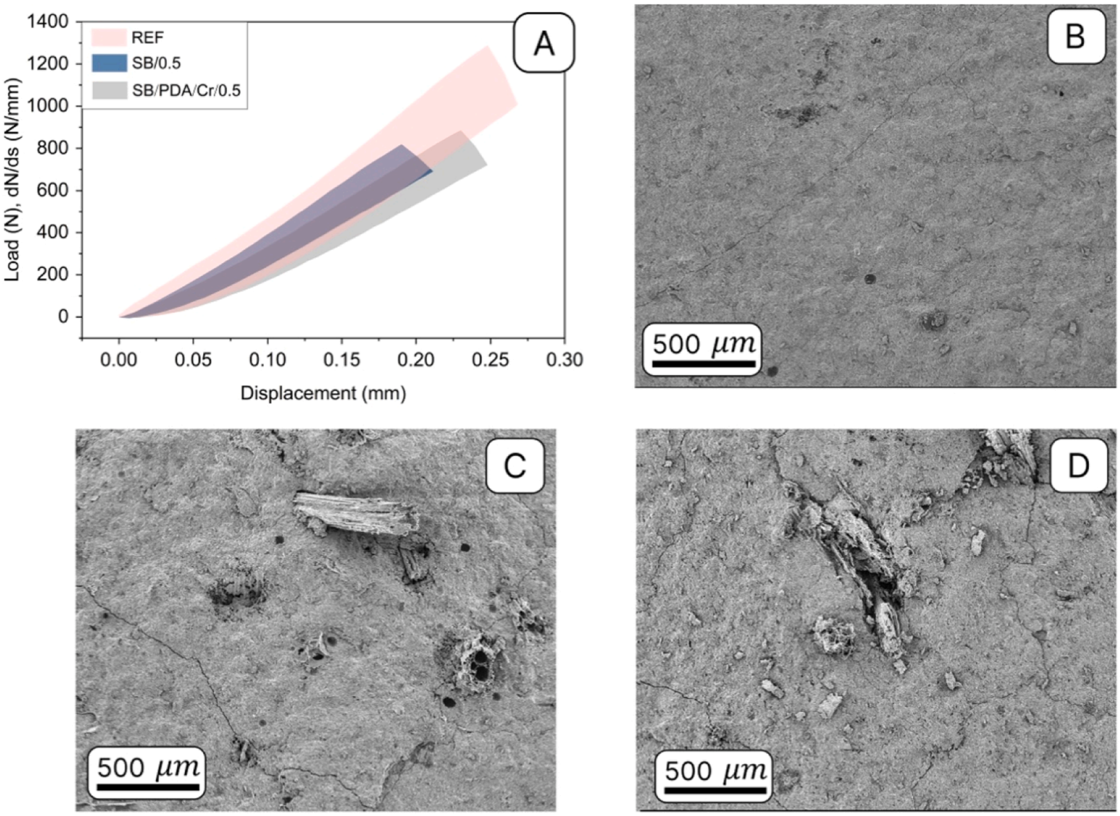

Fig. 7. . Load-displacement curves obtained for REF, SB/0.5, and SB/PDA/Cr/0.5 samples after 28 days curing (A), and SEM images of the fracture surface of REF (B), SB/0.5, (C) and SB/PDA/Cr/0.5 (D) samples.

and SB/PDA/Cr/0.5, Table 1) were analyzed by ICP-OES. Even after 64 days contact no leaching of chromium could be detected, suggesting that it was strongly retained in the cement phases. Considering the limit of detection of ICP OES ($0.4 - 2.0\ \mu g.L^{-1}$) (Hou and Jones, 2006), the risk of leaching Cr from the cement paste to the medium was discarded. Fig. 7**A** shows preliminary mechanical tests performed for the reference cement samples (REF), and for those containing 0.55 wt% of the fillers (SB/0.5 and SB/PDA/Cr/0.5). Turkey-Kramer test showed no statistically significant difference at type I error (α) of 0.05 (**Supplementary Material SM9**) among the data. Zein and coworkers observed that up to 1.0 wt% of spent adsorbent added to mortars did not affect the compressive strength value of the reference sample, but higher contents of adsorbents interfered with the hydration reaction and, consequently, reduced the compressive strength (Zein et al., 2022). Fig. 7**B–D** show the SEM images of the fracture surface of REF, SB/0.5, and SB/PDA/Cr/0.5 samples, respectively. The REF sample presented a smooth surface (Fig. 7**B**), whereas the surface of SB/0.5, and SB/PDA/Cr/0.5 samples evidenced the presence of SB microparticles (Fig. 7**B**) and SB/PDA agglomerates (Fig. 7**C**) distributed on the surface. The spent adsorbents seemed to be well integrated to the cement paste, and that might explain the low interference in the mechanical behavior.

4. Conclusions

PDA-modified SB microparticles were prepared by auto-oxidation of dopamine. The highest DA concentration led to adsorbents (SB/PDA4) with higher adsorption capacity. The fitting of the adsorption isotherms with the Khan model indicated a maximum adsorption capacity of 138.66 mg/g and heterogeneous adsorbent surface, as evidenced by SEM and AFM images. XPS spectra evidenced that the adsorption mechanism involves metal-ligand complexation, electrostatic interactions, and the reduction of Cr(VI) to Cr(III). The thermodynamic parameters revealed that the process was driven by an entropic gain. Fixed-bed column studies showed that columns packed with SB/PDA4 had good adsorption capacity towards Cr(VI) ions, achieving under optimal operational conditions (mass of adsorbent = 500 mg, $\nu = 1.5$ mL.min^{-1} and $C_0 = 150$ mg.L^{-1}) values as high as 141.70 mg.g^{-1}. The spent adsorbents could be immobilized in cement pastes at 0.5 wt%, minimizing environmental impact and contributing to the circular economy. For practical purposes, this study provided a sustainable adsorption process towards Cr(VI) adsorption and the valorization of the spent adsorbents.

Funding information

This work was supported by the São Paulo Research Foundation (FAPESP, grant 2021/07305–8 and 2018/13492–2) and Conselho Nacional de Pesquisa e Desenvolvimento (CNPq 304017–2021).

Declaration of Competing Interest

The authors declare that they have no known competing financial interests or personal relationships that could have appeared to influence the work reported in this paper.

Data availability

Data will be made available on request.

Acknowledgments

This work was supported by the São Paulo Research Foundation (FAPESP, grant 2021/07305–8 and 2018/13492–2) and Conselho

Nacional de Pesquisa e Desenvolvimento (CNPq 304017–2021). Acknowledgments to Natacha Cristina Faria for the training and support in the treatment of data from the mechanical resistance testing data. This research used facilities of the Brazilian Nanotechnology National Laboratory (LNNano), part of the Brazilian centre for Research in Energy and Materials (CNPEM), a private non-profit organization under the supervision of the Brazilian Ministry for Science, Technology, and Innovations (MCTI). The LNNano-XPS staff is acknowledged for the assistance during the experiments (XPS-20230821 and XPS-20221474).

Supplementary materials

Supplementary material associated with this article can be found, in the online version, at doi:10.1016/j.hazadv.2023.100366.

References

Ahmad, W., Ahmad, A., Ostrowski, K.A., Aslam, F., Joyklad, P., Zajdel, P., 2021. Sustainable approach of using sugarcane bagasse ash in cement-based composites: a systematic review. Case Stud. Constr. Mater. 15 (1), e00698.

Albadarin, A.B., Ala'a, H., Al-Laqtah, N.A., Walker, G.M., Allen, S.J., Ahmad, M.N.M., 2011. Biosorption of toxic chromium from aqueous phase by lignin: mechanism, effect of other metal ions and salts. Chem. Eng. J. 169 (1–3), 20–30.

Alsawy, T., Rashad, E., El-Qelish, M., Mohammed, R.H., 2022. A comprehensive review on the chemical regeneration of biochar adsorbent for sustainable wastewater treatment. NPJ Clean Water 5 (1), 29.

ASTM, 2008. Standard Test Method For Determination of the Point Load Strength Index of Rock and Application to Rock Strength Classifications. American Society for Testing and Materials West Conshohocken.

Ayawei, N., Ebelegi, A.N., Wankasi, D., 2017. Modelling and interpretation of adsorption isotherms. J. Chem. 2017 (1), 1–11.

Bagchi, D., Stohs, S.J., Downs, B.W., Bagchi, M., Preuss, H.G., 2002. Cytotoxicity and oxidative mechanisms of different forms of chromium. Toxicology 180 (1), 5–22.

Basha, S., Murthy, Z.V.P., 2007. Kinetic and equilibrium models for biosorption of Cr (VI) on chemically modified seaweed, Cystoseira indica. Process Biochem 42 (11), 1521–1529.

Baskar, A.V., Bolan, N., Hoang, S.A., Sooriyakumar, P., Kumar, M., Singh, L., Jasemizad, T., Padhye, L.P., Singh, G., Vinu, A., 2022. Recovery, regeneration and sustainable management of spent adsorbents from wastewater treatment streams: a review. Sci. Total Environ. 822 (1), 153555.

Bingül, Z., Irdemez, Ş., Demircioğlu, N., 2022. Effect of controlled and uncontrolled pH on tannery wastewater treatment by the electrocoagulation process. Int. J. Environ. Anal. Chem. 1, 1–16.

Chang, R., 2000. Physical Chemistry for the Chemical and Biological Sciences, third ed. University Science Books, California.

Charitha, V., Athira, V.S., Jittin, V., Bahurudeen, A., Nanthagopalan, P., 2021. Use of different agro-waste ashes in concrete for effective upcycling of locally available resources. Constr. Build. Mater. (285), 122851

Chen, C., Luo, M., Chen, F., Huang, C., Zhu, C., Wu, H., 2022a. Fe (III) complexed polydopamine modified Mg/Al layered double hydroxide enhances the removal of Cr (VI) from aqueous solutions. J. Polym. Environ. (30), 2547–2558.

Chen, C.T., Martin-Martinez, F.J., Jung, G.S., Buehler, M.J., 2017. Polydopamine and eumelanin molecular structures investigated with ab initio calculations. Chem. Sci. 8 (2), 1631–1641.

Chen, Q.Y., Tyrer, M., Hills, C.D., Yang, X.M., Carey, P., 2009. Immobilisation of heavy metal in cement-based solidification/stabilisation: a review. Waste Manag 29 (1), 390–403.

Chowdhury, M., Mostafa, M.G., Biswas, T.K., Mandal, A., Saha, A.K., 2015. Characterization of the effluents from leather processing industries. Environ. Process 2 (1), 173–187.

Cruz-Olivares, J., Pérez-Alonso, C., Martínez-Barrera, G., Roa-Morales, G., López-Téllez, G., del Campo-López, E.M., 2022. Modeling and scaling up of the Cr (VI) adsorption process by using mexicalcite natural mineral in a packed bed column. Results Eng. 16 (1), 100687.

Deng, J., Liu, Y., Li, H., Huang, Z., Qin, X., Huang, J., Zhang, X., Li, X., Lu, Q., 2022. A novel biochar-copolymer composite for rapid Cr (VI) removal: adsorption-reduction performance and mechanism. Sep. Purif. Technol. 295 (1), 121275.

Ding, Y., Weng, L.T., Yang, M., Yang, Z., Lu, X., Huang, N., Leng, Y., 2014. Insights into the aggregation/deposition and structure of a polydopamine film. Langmuir 30 (41), 12258–12269.

Do, D.D., 1998. Adsorption analysis: Equilibria and Kinetics (with cd Containing Computer MATLAB Programs). World Scientific Publishing, London.

Dong, L., Deng, R., Xiao, H., Chen, F., Zhou, Y., Li, J., Chen, S., Yan, B., 2019. Hierarchical polydopamine coated cellulose nanocrystal microstructures as efficient nanoadsorbents for removal of Cr (VI) ions. Cellulose 26 (1), 6401–6414.

Dreyer, D.R., Miller, D.J., Freeman, B.D., Paul, D.R., Bielawski, C.W., 2012. Elucidating the structure of poly (dopamine). Langmuir 28 (15), 6428–6435.

EA, NEN 7375., 2004. Leaching Characteristics of Moulded or Monolithic Building and Waste Materials Determination of Leaching of Inorganic Components with the Diffusion Test. In: The Tank Test. UK.

Elanchezhiyan, S.S.D., Sivasurian, N., Meenakshi, S., 2016. Enhancement of oil recovery using zirconium-chitosan hybrid composite by adsorptive method. Carbohydr. Polym. 145 (1), 103–113.

Erabeea, I.K., Ahsanb, A., Imteazc, M., Alomd, M.M., 2019. Adsorption of hexavalent chromium using activated carbon prepared from garden wastes. Desalin. Water Treat. 164 (1), 293–299.

Fu, F., Wang, Q., 2011. Removal of heavy metal ions from wastewaters: a review. J. Environ. Manag. 92 (3), 407–418.

Furtado, L.M., Ando, R.A., Petri, D.F.S., 2020. Polydopamine-coated cellulose acetate butyrate microbeads for caffeine removal. J. Mater. Sci. 55 (8), 3243–3258.

Furtado, L.M., Fuentes, D.P., Ando, R.A., Oliveira, P.V., Petri, D.F.S., 2022. Carboxymethyl cellulose/sugarcane bagasse/polydopamine adsorbents for efficient removal of Pb2+ ions from synthetic and undergraduate laboratory wastes. J. Clean. Prod. 380 (1), 134969.

Gao, H., Sun, Y., Zhou, J., Xu, R., Duan, H., 2013. Mussel-inspired synthesis of polydopamine-functionalized graphene hydrogel as reusable adsorbents for water purification. ACS Appl. Mater. Interfaces 5 (2), 425–432.

Gizaw, A., Zewge, F., Chebude, Y., Mekonnen, A., Tesfaye, M., 2022. Simultaneous nitrate and phosphate abatement using calcium silicate hydrate adsorbent: fixed bed column adsorption study. Surf. Interfaces 30 (1), 101961.

Hou, X., Jones, B.T., 2006. Inductively coupled plasma/optical emission spectrometry. Encyclopedia of analytical chemistry.In. In: Meyers, R.A. (Ed.), Encyclopedia of Analytical Chemistry, pp. 9468–9485.

Jin, X., Liu, Y., Tan, J., Owens, G., Chen, Z., 2018. Removal of Cr (VI) from aqueous solutions via reduction and absorption by green synthesized iron nanoparticles. J. Clean. Prod. 176 (1), 929–936.

Jittin, V., Bahurudeen, A., 2022. Evaluation of rheological and durability characteristics of sugarcane bagasse ash and rice husk ash based binary and ternary cementitious system. Constr. Build Mater. 317 (1), 125965.

Junior, H.S., Fiorelli, J., Dos Santos, S.F., 2017. Sustainable and Nonconventional Construction Materials Using Inorganic Bonded Fiber Composites. Woodhead Publishing, Cambridge.

Kesari, K.K., Soni, R., Jamal, Q.M.S., Tripathi, P., Lal, J.A., Jha, N.K., Siddiqui, M.H., Kumar, P., Tripathi, V., Ruokolainen, J., 2021. Wastewater treatment and reuse: a review of its applications and health implications. Water Air Soil Pollut. 232 (1), 1–28.

Khalfa, L., Cervera, M.L., Bagane, M., Souissi-Najar, S., 2016. Modeling of equilibrium isotherms and kinetic studies of Cr (VI) adsorption into natural and acid-activated clays. Arab. J. Geosci. 9 (1), 1–14.

Khan, A.R., Ataullah, R., Al-Haddad, A., 1997. Equilibrium adsorption studies of some aromatic pollutants from dilute aqueous solutions on activated carbon at different temperatures. J. Colloid Interface Sci. 194 (1), 154–165.

Khan, M.M., Khan, A., Bhatti, H.N., Zahid, M., Alissa, S.A., El-Badry, Y.A., Hussein, E.E., Iqbal, M., 2021. Composite of polypyrrole with sugarcane bagasse cellulosic biomass and adsorption efficiency for 2, 4-dicholrophonxy acetic acid in column mode. J. Mater. Res. 15 (1), 2016–2025.

Kumar, A., Kumar Tripathi, V., Sachan, P., Rakshit, A., Singh, R.M., Shukla, S.K., Pandey, R., Vishwakarma, A., Panda, K.C., Madhav, S., Kanhaiya, S., Srivastav, A., Singh, V., Singh, P., 2022. Chapter 10 - sources of ions in the river ecosystem. Ecological Significance of River Ecosystems. Elsevier, pp. 187–202.

Kumari, R., Dey, S., 2019. A breakthrough column study for removal of malachite green using coco-peat. Int. J. Phytoremediation 21 (12), 1263–1271.

Li, P., Fu, T., Gao, X., Zhu, W., Han, C., Liu, N., He, S., Luo, Y., Ma, W., 2019. Adsorption and reduction transformation behaviors of Cr(VI) on mesoporous polydopamine/titanium dioxide composite nanospheres. J. Chem. Eng. Data 64 (6), 2686–2696.

Li, R., An, Q.D., Mao, B.Q., Xiao, Z.Y., Zhai, S.R., Shi, Z., 2017. PDA-meditated green synthesis of amino-modified, multifunctional magnetic hollow composites for Cr (VI) efficient removal. J. Taiwan Inst. Chem. Eng. 80 (1), 596–606.

Liebscher, J., Mrówczyński, R., Scheidt, H.A., Filip, C., Hădade, N.D., Turcu, R., Bende, A., Beck, S., 2013. Structure of polydopamine: a never-ending story? Langmuir 29 (33), 10539–10548.

Liu, F., Jamal, R., Abdiryim, T., Liu, X., 2022. Polydopamine-based polysaccharide materials for water treatment. Cellulose 29 (15), 8025–8064.

Luo, X., Du, H., Zhang, X., Yang, Y., 2022. Amine-functionalized magnetic biochars derived from invasive plants Alternanthera philoxeroides for enhanced efficient removal of Cr (VI): performance, kinetics and mechanism studies. Environ. Sci. Pollut. Res. 29 (51), 78092–78106.

Lv, D., Zhou, J., Cao, Z., Xu, J., Liu, Y., Li, Y., Yang, K., Lou, Z., Lou, L., Xu, X., 2019. Mechanism and influence factors of chromium (VI) removal by sulfide-modified nanoscale zerovalent iron. Chemosphere 224, 306–315.

Ma, B., Yao, J., Chen, Z., Liu, B., Kim, J., Zhao, C., Zhu, X., Mihucz, V.G., Minkina, T., Knudsen, T.Š., 2022. Superior elimination of Cr(VI) using polydopamine functionalized attapulgite supported nZVI composite: behavior and mechanism. Chemosphere 287 (1), 131970.

Mangwandi, C., Kurniawan, T.A., Albadarin, A.B., 2020. Comparative biosorption of chromium (VI) using chemically modified date pits (CM-DP) and olive stone (CM-OS): kinetics, isotherms and influence of co-existing ions. Chem. Eng. Res. Des. 156 (1), 251–262.

Meneses, I.P., Novaes, S.D., Dezotti, R.S., Oliveira, P.V., Petri, D.F.S., 2022. CTAB-modified carboxymethyl cellulose/bagasse cryogels for the efficient removal of bisphenol A, methylene blue and Cr (VI) ions: batch and column adsorption studies. J. Hazard. Mater. 421 (1), 126804.

Mohan, D., Pittman, C.U., 2007. Arsenic removal from water/wastewater using adsorbents—a critical review. J. Hazard. Mater. 142 (1–2), 1–53.

Nasruddin, M.N., Fahmi, M.R., Abidin, C.Z.A., Yen, T.S., 2018. Regeneration of Spent Activated Carbon from wastewater treatment plant application. J. Phys. Conf. Ser. 11116 (1), 032022.

Nithya, R., Gomathi, T., Sudha, P.N., Venkatesan, J., Anil, S., Kim, S.K., 2016. Removal of Cr (VI) from aqueous solution using chitosan-g-poly (butyl acrylate)/silica gel nanocomposite. Int. J. Biol. Macromol. 87 (1), 545–554.

Novaes, S.D., Oliveira, P.V., Petri, D.F.S., 2022. Hydroxypropyl methylcellulose-sugarcane bagasse adsorbents for removal of 17α-ethinylestradiol from aqueous solution and freshwater. Environ. Sci. Pollut. Res. 29 (42), 1–17.

Pholosi, A., Naidoo, E.B., Ofomaja, A.E., 2020. Batch and continuous flow studies of Cr (VI) adsorption from synthetic and real wastewater by magnetic pine cone composite. Chem. Eng. Res. Des. 153 (1), 806–818.

Rajapaksha, A.U., Selvasembian, R., Ashiq, A., Gunarathne, V., Ekanayake, A., Perera, V. O., Wijesekera, H., Mia, S., Ahmad, M., Vithanage, M., 2022. A systematic review on adsorptive removal of hexavalent chromium from aqueous solutions: recent advances. Sci. Total Environ. 809 (1), 152055.

Ryu, J.H., Messersmith, P.B., Lee, H., 2018. Polydopamine surface chemistry: a decade of discovery. ACS Appl. Mater. Interfaces 10 (9), 7523–7540.

Sarker, T.C., Azam, S.M.G.G., El-Gawad, A.M.A., Gaglione, S.A., Bonanomi, G., 2017. Sugarcane bagasse: a potential low-cost biosorbent for the removal of hazardous materials. Clean Technol. Environ. Policy 19 (1), 2343–2362.

Sharma, A., Rana, H., Goswami, S., 2022. A comprehensive review on the heavy metal removal for water remediation by the application of lignocellulosic biomass-derived nanocellulose. J. Polym. Environ. 30 (1), 1–18.

Shokouhfar, N., Aboutorabi, L., Morsali, A., 2018. Improving the capability of UiO-66 for Cr (VI) adsorption from aqueous solutions by introducing isonicotinate N-oxide as the functional group. Dalton Trans. 47 (41), 14549–14555.

Silverstein, R.M., Bassler, G.C., 1962. Spectrometric identification of organic compounds. J. Chem. Educ. 39 (11), 546.

Simón, D., Palet, C., Costas, A., Cristóbal, A., 2022. Agro-industrial waste as potential heavy metal adsorbents and subsequent safe disposal of spent adsorbents. Water 14 (20), 3298.

Srivastava, S., Agrawal, S.B., Mondal, M.K., 2019. Fixed bed column adsorption of Cr (VI) from aqueous solution using nanosorbents derived from magnetite impregnated Phaseolus vulgaris husk. Environ. Prog. Sustain. Energy 38 (s1), S68–S76.

Sulistiyo, C.D., Cheng, K.C., Su'andi, H.J., Yuliana, M., Hsieh, C.W., Ismadji, S., Angkawijaya, A.E., Go, A.W., Hsu, H.Y., Tran-Nguyen, P.L., 2022. Removal of hexavalent chromium using durian in the form of rind, cellulose, and activated carbon: comparison on adsorption performance and economic evaluation. J. Clean Prod. 380 (1), 135010.

Sun, X., Imai, T., Sekine, M., Higuchi, T., Yamamoto, K., Kanno, A., Nakazono, S., 2014. Adsorption of phosphate using calcined Mg3–Fe layered double hydroxides in a fixed-bed column study. J. Ind. Eng. Chem. 20 (5), 3623–3630.

Thomas, H.C., 1944. Heterogeneous ion exchange in a flowing system. J. Am. Chem. Soc. 66 (10), 1664–1666.

Verma, R., Maji, P.K., Sarkar, S., 2021. Comprehensive investigation of the mechanism for Cr (VI) removal from contaminated water using coconut husk as a biosorbent. J. Clean Prod. 314 (1), 128117.

Wan, C., Zhang, R., Wang, L., Liu, X., Bao, D., Song, G., 2021. Enhanced reduction and *in-situ* stabilization of Cr (VI) by Fe3O4@ polydopamine magnetic microspheres embedded in sludge-based carbonaceous matrix. Appl. Surf. Sci. 536 (1), 147980.

Wang, H., Wang, Z., Yue, R., Gao, F., Ren, R., Wei, J., Wang, X., Kong, Z., 2020. Rapid preparation of adsorbent based on mussel inspired chemistry and simultaneous removal of heavy metal ions in water. Chem. Eng. J. 383 (1), 123107.

Wang, J., Guo, X., 2020. Adsorption kinetic models: physical meanings, applications, and solving methods. J. Hazard. Mater. 390 (1), 122156.

Wei, Z., Zhang, S., Wang, X., Long, S., Yang, J., 2021. A high Cr (VI) absorption efficiency and easy recovery adsorbent: electrospun polyethersulfone/polydopamine nanofibers. J. Appl. Polym. Sci. 138 (27), 50642.

Xiang, L., Lin, J., Yang, Q., Lin, S., Chen, S., Yan, B., 2020. Facile preparation of hierarchical porous polydopamine microspheres for rapid removal of chromate from the wastewater. J. Leather Sci. Eng. 2 (1), 1–10.

Xu, C., Xu, Y., Zhong, D., Chang, H., Mou, J., Wang, H., Shen, H., 2023. Zr4+ and glutaraldehyde cross-linked polyethyleneimine functionalized chitosan composite: synthesis, characterization, Cr (VI) adsorption performance, mechanism and regeneration. Int. J. Biol. Macromol. 239 (1), 124266.

Xu, J., Li, H., Lowry, G.V., 2021. Sulfidized nanoscale zero-valent iron: tuning the properties of this complex material for efficient groundwater remediation. Acc. Mater. Res. 2 (6), 420–431.

Yahya, M.D., Abubakar, H., Obayomi, K.S., Iyaka, Y.A., Suleiman, B., 2020. Simultaneous and continuous biosorption of Cr and Cu (II) ions from industrial tannery effluent using almond shell in a fixed bed column. Results Eng. 6 (1), 100113.

Yakout, S., Hassan, M., Omar, H., 2019. Fixed-bed column study for the removal of hexavalent chromium ions from aqueous solutions via pyrolysis of the rice husk. Desalin. Water Treat. 170 (1), 128–137.

Yang, Q., Wang, H., Li, F., Dang, Z., Zhang, L., 2021. Rapid and efficient removal of Cr (vi) by a core–shell magnetic mesoporous polydopamine nanocomposite: roles of the mesoporous structure and redox-active functional groups. J. Mater. Chem. A Mater. 9 (22), 13306–13319.

Zein, R., Fauzia, S., Bielan, Z., Aziz, H., Dahlan, D., Konieczka, P., Cieślik, B.M., 2022. Analytical chemistry in technical approaches: immobilization of biosorbent waste containing heavy metals in cemented materials. Monatsh. für Chem. 153 (9), 789–800.

Zhang, P., Zou, K., Yuan, L., Liu, J., Liu, B., Qing, T.P., Feng, B., 2022. A biomass resource strategy for alginate-polyvinyl alcohol double network hydrogels and their adsorption to heavy metals. Sep. Purif. Technol. 301 (1), 122050.

Zhang, Q., Li, Y., Yang, Q., Chen, H., Chen, X., Jiao, T., Peng, Q., 2018. Distinguished Cr (VI) capture with rapid and superior capability using polydopamine microsphere: behavior and mechanism. J. Hazard. Mater. 342 (1), 732–740.

Zhu, H., Wu, J., Fang, M., Tan, L., Chen, C., Alharbi, N.S., Hayat, T., Tan, X., 2017. Synthesis of a core–shell magnetic Fe 3 O 4–NH 2@ PmPD nanocomposite for efficient removal of Cr(VI) from aqueous media. RSC Adv. 7 (58), 36231–36241.

Zoghlami, A., Paës, G., 2019. Lignocellulosic biomass: understanding recalcitrance and predicting hydrolysis. Front. Chem. 7 (1), 874.